Estimation of seismic centroid moment tensor using ocean bottom pressure gauges as seismometers

Tatsuya Kubota[1], Tatsuhiko Saito[1], Wataru Suzuki[1], and Ryota Hino[2]

[1]National Research Institute for Earth Science and Disaster Resilience, Tsukuba, Japan.

[2]Graduate School of Science, Tohoku University, Sendai, Japan.

Corresponding author: Tatsuya Kubota (kubotatsu@bosai.go.jp)

Key Points:

- We estimated the CMT of offshore M ~ 7 earthquak es using onshore seismometers and offshore pressure gauges
- The horizontal location of the centroid is well constrained by using offshore pressure gauges as seismometers
- Observed pressure-change waveforms show the theoretical predicted relationship between pressure and vertical acceleration

Abstract

We examined the dynamic pressure change at the seafloor to estimate the centroid moment tensor solutions of the largest and second largest foreshocks (Mw 7.2 and 6.5) of the 2011 Tohoku-Oki earthquake. Combination of onshore broadband seismograms and high-frequency (~20–200 s) seafloor pressure records provided the resolution of the horizontal locations of the centroids, consistent with the results of tsunami inversion using the long-period (> ~10 min) seafloor pressure records although the depth was not constrained well, whereas the source locations were poorly constrained by the onshore seismic data alone. Also, the waveforms synthesized from the estimated CMT solution demonstrated the validity of the theoretical relationship between pressure change and vertical acceleration at the seafloor. The results of this study suggest that offshore pressure records can be utilized as offshore seismograms, which would be greatly useful for revealing the source process of offshore earthquakes.

1. Introduction

When earthquakes occur offshore, associated tsunami are observed by ocean-bottom pressure gauges (OBPGs). For example, the DART (Deep-ocean Assessment and Reporting of Tsunamis) systems developed by NOAA (National Oceanic and Atmospheric Administration) were founded on a network of widely distributed OBPGs to monitor tsunami far offshore (e.g., González et al., 2005). OBPGs are considered one of the most reliable sensors for investigating tsunami propagation and source models because they are free from the strong site effects usually observed near coasts. Near-field (less then ~100 km from the epicenters) OBPG tsunami records enable us to obtain good spatial resolution of the source models of offshore moderate (M ~ 7) earthquakes (e.g., Saito et al., 2010; Kubota et al., 2015; 2017). Lack of resolution for source models will be a barrier for studying the detailed source processes of offshore earthquakes (e.g., Heiderzadeh et al., 2017a).

Near-field pressure records obtained ~20 km from two local earthquakes (Mw 7.2 and Mw 6.5, National Research Institute for Earth Science and Disaster Resilience [NIED], 2011a; 2011b) (the station and earthquake locations are in Figure 1) are shown in Figure 2. By applying a low-pass filter (>400 s) to the original records (gray), we obtained clear tsunami signals (blue). The maximum tsunami height was ~10 cm (Figure 2b) and ~1 cm (Figure 2e) for the Mw 7.2 and 6.5 earthquakes, respectively. Some studies have estimated earthquake fault models by analyzing such tsunami signals in the OBPGs (e.g., Gusman et al., 2013; Heidarzadeh et al., 2017b; Kubota et al. 2017).

In addition to tsunami, OBPGs can observe other signals associated with earthquakes. When OBPGs are installed inside the focal area, permanent seafloor vertical deformations are observed as the difference between the average pressure levels before and after the earthquake. These are often used to estimate coseismic fault models (e.g., Ito et al., 2011; 2013; Iinuma et al., 2012; Ohta et al., 2012; Tsushima et al., 2012; Wallace et al., 2016). The pressure changes associated with tsunami and permanent deformations are interpreted as the change in the loading due to the water column over the OBPG based on the hydrostatic assumption. OBPGs also observe dynamic pressure changes associated with seismic waves (e.g., Filloux, 1982; Bolshakova et al., 2011; Matsumoto et al., 2012; Saito & Tsushima, 2016), which are caused by seafloor seismic motions and ocean acoustic waves. In Figure 2, high-frequency pressure changes are evident from large amplitudes, especially after applying a bandpass filter with a passband of 0.01–0.05 Hz (red lines). These components are usually removed before tsunami waveform analyses (e.g., Gusman et al., 2013; Inazu & Saito, 2014; Kubota et al., 2015; 2017; Heidarzadeh et al., 2016), because they are irrelevant to the sea surface displacement due to tsunami.

The dynamic pressure change associated with seismic motion has been previously studied (e.g., Filloux, 1982; Nosov & Kolesov, 2007; Bolshakova et al., 2011; Matsumoto et al., 2012; Saito, 2013). The pressure changes can be interpreted based on two different relationships according to their frequency range, defined by the fundamental acoustic resonant frequency $f_0 = c_0/4h_0$ (h_0 is the water depth and c_0 is the velocity of the ocean acoustic wave). When the frequency of the seafloor motion is sufficiently low compared to the fundamental acoustic resonant frequency f_0 ($f < f_0$), the seafloor pressure change can be approximated as:

$$p = \rho_0 h_0 a_z, \tag{1}$$

and when the frequency is high ($f > f_0$) as:

$$p = \rho_0 c_0 v_z, \tag{2}$$

where ρ_0 is seawater density and a_z and v_z are the vertical acceleration and velocity of the seafloor motion (hereafter, pressure–acceleration relationship and pressure–velocity relationship), respectively (e.g., Bolshakova et al., 2011; Matsumoto et al., 2012). Numerical simulation is useful for investigating these relationships (e.g., Maeda et al., 2013; Kozdon & Dunham, 2014; Saito & Tsushima, 2016; Saito, 2017). Saito and Tsushima (2016) tried to reproduce the dynamic pressure change associated with the 2011 Tohoku-Oki earthquake by numerical simulation, assuming a uniform slip fault model. The simple model roughly reproduced the dynamic pressure changes, but not completely. Using the seismic equations considering a compressible sea and elastic crust, Saito (2017) numerically simulated the vertical acceleration and pressure at the seafloor, and found that the pressure–acceleration relationship (equation (1)) works well, whereas the pressure–velocity relationship (equation (2)) works only for the first motion of the pressure change.

Although many previous studies have investigated the pressure–acceleration relationship (equation (1)) based on theoretical studies or numerical simulations, there are few studies based on real observations. Matsumoto et al. (2012) showed the pressure–

acceleration relationship works reasonably well in the frequency domain by comparing records of the Tohoku-Oki earthquake observed ~400 km away from the focal area. Nosov and Kolesov (2007) also investigated pressure records of the 2003 Tokachi-Oki earthquake (Mw 8.0), but only in the frequency domain. Those studies did not compare records in the time domain. Hence, it is not confirmed whether the phases are in agreement or have some shift in the time domain. If the pressure–acceleration relationship works well in the time domain, we could estimate various earthquake parameters by applying seismological analyses to the pressure data.

The purpose of this study is to clarify whether the pressure–acceleration relationship holds in observed records through a centroid moment tensor (CMT) analysis of offshore earthquakes. Moreover, we demonstrate that the use of offshore OBPG records improves the centroid horizontal locations of the offshore earthquakes.

2. Ocean Bottom Pressure Data

We used pressure data associated with the Mw 7.2 and 6.5 interplate earthquakes off northeastern Japan on 9 March, 2011, which were the largest and second largest events preceding the 2011 Tohoku-Oki earthquake (Ohta et al., 2012; Gusman et al., 2013; Kubota et al., 2017) (hereafter foreshock #1, foreshock #2, and the mainshock, respectively). Since the magnitudes of the two foreshocks were large enough to show good signal-to-noise ratios, the source processes are relatively simple compared to the mainshock, and we can expect to obtain a reasonable CMT solution with a point-source assumption. Also, the rupture areas of these earthquakes have been estimated from tsunami data by Kubota et al. (2017) (colored rectangles in Figure 1), and those estimates can be used as a reference for validating the centroid location.

We used 1 Hz sampled pressure data. Seven offline autonomous OBPGs with pop-up recovery were deployed within ~70 km of the epicenters (Figure 1). Details are given in Hino et al. (2014). Real-time cabled OBPGs of the Earthquake Research Institute of the University of Tokyo (Kanazawa & Hasegawa, 1997), TM1 and TM2, were also in operation more than 100 km away from the epicenters (Figure 1).

Figure 3 shows the original and bandpass-filtered pressure records. We applied the Butterworth-type bandpass filter in both the forward and reverse directions. The passband was determined according to the fundamental resonant frequency f_0 and the frequency range used in the F-net Moment Tensor (MT) analysis by the National Research Institute for Earth Science and Disaster Resilience (NIED, 2011a; 2011b). Supposing the acoustic wave velocity c_0 = 1.5 km/s and the water depth h_0 = 1.5 km (average depth of the focal area), the fundamental resonant frequency ($f_0 = c_0/4h_0$) is ~0.25 Hz (4 s). If the sea depth is 3.2 km (corresponding to the depth of the deepest OBPG, GJT3), f_0 is ~0.12 Hz (8.5 s). Since the pressure–acceleration relationship holds when the dominant frequency is lower than the acoustic resonant frequency ($f < f_0$), the high-frequency component ($f >$ ~0.1 Hz) should be suppressed. As for the low-frequency cutoff, tsunami components ($T >$ ~400 s, $f <$ ~0.0025 Hz) should be reduced. The F-net MT analysis adopted a passband of 0.005–0.02 Hz (50–200 s) for foreshock #1, and 0.01–0.05 Hz (20–100 s) for foreshock #2 (NIED, 2011a; 2011b). Considering the factors above, we took the passband to be 0.005–0.02 Hz for foreshock #1, and 0.01–0.05 Hz for foreshock #2.

3. Methodology and Results: Centroid Moment Tensor Inversion using Dynamic Pressure Records

We estimated the centroid moment tensors, centroid times, and centroid locations of the two earthquakes by analyzing onshore seismic and offshore dynamic pressure data. The procedure for the CMT inversion followed the grid-search approach of Ito et al. (2006), which uses five independent basis MT components (Kikuchi & Kanamori, 1991) (details of the calculation of Green's functions and the CMT inversion are given in Text S1). In the analysis, the seafloor vertical acceleration is calculated using a conventional elasto-dynamic equation using the discrete wavenumber method (e.g., Saikia, 1994) with the 1-D subsurface structure model of Kubo et al. (2002), and is converted to the dynamic pressure change using the pressure–acceleration relationship (equation (1)), where the water density ρ_0 is set as 1.03 g/cm^3. The sea depths h_0 of the OBPGs are summarized in Table S1. The same bandpass filter used for the observation is applied to the calculated waveforms. As a measure of waveform reproducibility, we used variance reduction (VR):

$$VR = \left(1 - \frac{\sum_{k=1}^{N}\left(w_k d_k^{obs} - w_k d_k^{calc}\right)^2}{\sum_{k=1}^{N}\left(w_k d_k^{obs}\right)^2}\right) \times 100\ (\%) \tag{3}$$

where d_k^{obs} and d_k^{calc} are the k-th data of observed and calculated waveforms, respectively, and N denotes the number of data used for inversion. Note that the onshore seismometers and offshore OBPGs have different dimensions. To reduce the bias caused by the difference in the inversion analysis, we introduced the weight value, w_k, as the inverse of the maximum amplitude of each waveform:

$$w_k = \frac{1}{\max\left(d_i(t)\right)}, \tag{4}$$

where $d_i(t)$ is the time series of the i-th station including the k-th datum. With respect to the grid search, we sought the horizontal and vertical locations of the centroid at 0.1° intervals in the horizontal and 2 km in the vertical. The interval of the temporal grids is 1 s.

In the analysis, we used two types of datasets, as follows. One of the datasets consists only of the onshore seismograms (dataset 1). Three (radial, transverse, and vertical) velocity components were obtained by the F-net stations (e.g., Okada et al., 2004). We analyzed the same datasets used in the F-net MT solution: the F-net stations NOP, WJM, and WTR for foreshock #1 (NIED, 2011a, red triangles in Figure 1) and IMG, KZK, and SGN for foreshock #2 (NIED, 2011b, blue triangles). We prepared another dataset (dataset 2) by adding the pressure data obtained at GJT3, which is located on the offshore side of the epicenters, to dataset 1, in order to improve the station coverage.

The estimated CMT solutions of foreshock #1 are shown in Figure 4. Using only the onshore seismograms (dataset 1), the centroid of foreshock #1 was estimated at 143.2°E, 38.4°E, and 30 km with a VR of 66.1% (gray CMT solution in Figure 4a). The strike, dip, and rake were 171.2°, 21.2°, and 52.0°, respectively, and the seismic moment M_0 was 5.5 × 10^{19} Nm (Mw 7.1). This solution was close to the F-net solution in location and mechanism (143.2798°E, 38.3285°E, 23 km, and 8.9 × 10^{19} Nm; black CMT solution in Figure 4a) (NIED, 2011a). The centroid was not located inside the rupture area estimated by the tsunami waveform analysis (Kubota et al., 2017) (red rectangle in Figure 4b).

On the other hand, using dataset 2 (pressure data from GJT3 included), the centroid was estimated at 142.9°E, 38.5°E, and 30 km (red CMT solution in Figure 4b) with a VR of

61.9%; the strike, dip, and rake were 164.1°, 23.2°, and 44.1°, respectively, and M_o = 5.1 × 10^{19} Nm (M_W 7.1). The centroid was located almost at the center of the rupture area obtained from tsunami waveform inversion (Kubota et al., 2017).

We conducted forward simulations of OBPG waveforms not used for the inversion, to examine the agreement with and observation. Both CMT solutions estimated from dataset 1 and dataset 2 reproduced the seismograms of the F-net stations nicely (Figure 4c), suggesting that the difference in the centroid horizontal locations cannot be resolved using only the seismograms of onshore stations. In contrast, we recognize the difference in the pressure waveforms recorded at offshore stations. The waveforms obtained from dataset 2 (red lines in Figure 4d) reproduce the observations (black) better than those from dataset 1 (gray). Note that we used only GJT3 in the inversion analysis, but we also see this improvement in other pressure records. For example, if we evaluate the VR of P09 (VR_{P09}) using the same time window used for inversion (white background area in Figure 4d), we obtained 2.5% for the CMT solution from dataset 1 and 70.6% for the solution of dataset 2.

We obtained similar results for foreshock #2. The centroid location of foreshock #2 obtained from dataset 1 was 143.2°E, 38.2°E, and 26 km with a VR of 80.1% (gray CMT solution in Figure 5a), and the strike, dip, and rake were 194.0°, 19.1°, and 77.3°, respectively (M_o = 4.2 × 10^{18} Nm, Mw 6.4). These are similar to the F-net solution (black) of 143.0448°E, 38.1722°E, and 20 km (M_o = 5.51 × 10^{18} Nm) (NIED, 2011b). When GJT3 was included (dataset 2), the centroid was at 142.9°E, 38.3°E, and 32 km with a VR of 68.8%, and the strike, dip and rake were 144.1°, 39.2°, and 21.1°, respectively (M_o = 4.2 × 10^{19} Nm, Mw 6.4) (Figure 5b). We found that the centroid estimated from dataset 2 was closer to the center of the fault model than that from dataset 1. Also, the CMT solution estimated using dataset 2 reproduced the OBPG records better: the values of VR_{P09} were −13.6% (dataset 1) and 48.0% (dataset 2).

To evaluate the resolution and accuracy of the centroid horizontal location, we calculated the area where the VR exceeds 90% of the best-fit VR in each result. The high-VR area (>90%) is surrounded by gray lines in Figures 4a, 4b, 5a, and 5b. For both foreshocks #1 and #2, the high-VR area extended in the ENE–WSW direction when pressure records from GJT3 were not used for the inversion (dataset 1) by ~100 km and ~50 km, respectively (Figures 4a and 5a), suggesting the horizontal location of the centroid is not well constrained.

On the other hand, the high-VR area obtained from dataset 2 was much smaller and the EW extent of the high-VR area became by half (by ~50 km for foreshock #1 and ~25 km for foreshock #2), and mostly confined within the spatial extent of the finite fault models derived by the tsunami inversion (Figures 4b and 5b). Since the station coverage was improved by adding the dynamic pressure obtained at GJT3, located on the offshore side of the focal area (Figure 1), the resolution of the centroid horizontal location was significantly improved.

The obtained centroid depths (~30 km) are systematically deeper than the plate boundary depth obtained by the seismic survey (Ito et al., 2005). To discuss the depth resolution, we examined the vertical VR distribution at the horizontal point where the best-fit CMT is obtained (Figures S1 and S2). When the centroid depth is less than ~10 km, the VR is smaller than 90% of the maximum VR, suggesting that the centroid depth is deeper than 10 km. However, the vertical range where the VR exceeds 90% of the best value (gray lines in Figures S1 and S2) is widely distributed, suggesting the centroid depths are not well constrained. We also point out that that the centroid depths and the centroid time delay have a trade-off relationship.

4. Discussion

4.1. Checking the validity of the pressure–acceleration relationship

Past studies have found that the seismograms and pressure records in the Fourier amplitude are consistent with the theoretical relationship given by equation (1) (e.g., Matsumoto et al., 2012). However, equation (1) suggests not only an agreement in the Fourier amplitude but also in the time series of the accelerograms and pressure records. It is important to confirm the agreement in the waveforms by observations. Our results confirmed equation (1) by indirect comparison of the waveforms: the observed pressure records and theoretically calculated accelerograms. In Figures 4d and 5d, we compare the observed pressure records and pressure changes converted from the calculated accelerograms based on equation (1). The theoretically predicted pressure changes (red and blue lines) agree well with the observations (gray lines) at stations P02, P06, and P09, although those data were not used in the inversion analysis. Hence, the agreement found in those waveforms strongly supports the validity of equation (1) in time domain. Disagreement at station P08 may be caused by insufficient modeling using the point-source approximation near the finite-fault source.

4.2. Importance of offshore dynamic pressure change for source estimation

Our results show that OBPGs are very useful in constraining centroid horizontal locations. This is mainly because of the improvement in station coverage achieved by using the pressure data as offshore seismograms. A high sampling rate (1 Hz) also contributes to obtaining the CMT solution. Filloux (1982) has already suggested the applicability of seafloor pressure data as seismometers, but the sampling rate in his analysis was very low (28 s). If the sampling rate is low, aliasing due to the higher-frequency ocean acoustic wave (with a dominant period of ~5–10 s) may prevent us from obtaining high-quality bandpass filtered waveforms. The use of 1-Hz-sampling pressure data enabled us to use high-quality seismograms for CMT analysis. The dynamic pressure records, free from amplitude saturation, can be treated as on-scale near-field seismic records of offshore large earthquakes, as demonstrated here. As mentioned by Heidarzadeh et al. (2017a), lack of resolution for source models of offshore moderate earthquakes will make it difficult to investigate the detailed source processes. It is expected that broadband seismograms provided by OBPGs will contribute to estimating earthquake source processes in future studies, such as the finite fault model or source duration. The source duration would be useful for identifying tsunami earthquakes. The investigation of more examples would be necessary to confirm the applicability of OBPGs as the broadband seismometer in more detail (e.g., lower limit of the analyzable magnitude range).

5. Conclusions

Using the dynamic pressure data observed by OBPGs deployed near the focal area together with onshore seismograms, we estimated CMT solutions for two moderate (M ~ 7) offshore interplate earthquakes, and evaluated the robustness of the estimation of the horizontal centroid location. When offshore OBPG data were excluded, the horizontal location of the centroid was not well resolved, and the best-fit centroid was estimated outside of the rupture areas obtained by a previous study. Meanwhile, the centroid locations were well resolved and reasonably constrained inside the rupture area when we used both onshore seismograms and offshore OBPGs, although the depth resolution were not so good in the present study. The extent of the area where relatively high VRs were obtained (i.e., estimation error) became around half by adding offshore OBPG record. Also, by using the estimated CMT solution, we successfully simulated the actual observed ocean-bottom pressure change records, except for a few stations near the source. The results of our study indicate that the theoretical relationship of equation (1) is valid for actual observations, and we can improve the source estimation of offshore earthquakes using OBPGs based on equation (1).

Acknowledgments, Samples, and Data

The authors are grateful to Earthquake Research Institute, the University of Tokyo and Earthquake and Volcano Hazards Observation and Research Program, the Ministry of Education, Culture, Sports, Science and Technology (MEXT) of Japan for providing seafloor pressure data. This study was supported by the research project "Research concerning Interaction between the Tokai, Tonankai, and Nankai Earthquakes" of MEXT, and by JSPS KAKENHI Grant Numbers JP20244070, JP26000002, and JP15K17752. The authors declare that they have ho competing interests. The figures in this paper were prepared using Generic Mapping Tools (GMT) (Wessel & Smith, 1998). The authors thank the editor Andrew V. Newman and the reviewers Mohammad Heidarzadeh of Brunel University, London, and Yoshihiro Ito of Kyoto University, Japan, for helpful comments, which improved the manuscript. The F-net waveform data and MT solutions are available at the website of the National Research Institute for Earth Science and Disaster Resilience (NIED), Japan (http://www.fnet.bosai.go.jp/top.php?LANG=en). The OBPG data used in this study are available in the supplementary datasets S1, S2, and S3 (the description of the datasets is in Text S2).

References

Bolshakova, A., Inoue, S., Kolesov, S., Matsumoto, H., Nosov, M., & Ohmachi, T. (2011). Hydroacoustic effects in the 2003 Tokachi-oki tsunami source. *Russian Journal of Earth Sciences*, *12*, ES2005. doi:10.2205/2011ES000509

Filloux, J. H. (1982). Tsunami recorded on the open ocean floor. *Geophysical Research Letters*, *9*(1), 25–28. doi:10.1029/GL009i001p00025

González, F. I., Bernard, E. N., Meinig, C., Eble, M. C., Mofjeld, H. O., & Stalin, S. (2005). The NTHMP tsunameter network. *Natural Hazards*, *35*, 25–39. doi:10.1007/s11069-004-2402-4

Gusman, A. R., Fukuoka, M., Tanioka, Y., & Sakai, S. (2013). Effect of the largest foreshock (Mw 7.3) on triggering the 2011 Tohoku earthquake (Mw 9.0). *Geophysical Research Letters*, *40*, 497–500. doi:10.1002/grl.50153

Heidarzadeh, M., Harada, T., Satake, K., Ishibe, T., & Gusman, A. (2016). Comparative study of two tsunamigenic earthquakes in the Solomon Islands: 2015 Mw 7.0 normal-fault and 2013 Santa Cruz Mw 8.0 megathrust earthquakes. *Geophysical Research Letters*, *43(9)*, 4340–4349. doi:10.1002/2016GL068601

Heidarzadeh, M., Harada, T., Satake, K., Ishibe, T., & Takagawa, T. (2017a). Tsunamis from strike-slip earthquakes in the Wharton Basin, northeast Indian Ocean: March 2016 Mw 7.8 event and its relationship with the April 2012 Mw 8.6 event. *Geophysical Journal International*, accepted. doi:10.1093/gji/ggx395

Heidarzadeh, M., Murotani, S., Satake, K., Takagawa, T., & Saito, T. (2017b). Fault size and depth extent of the Ecuador earthquake (Mw 7.8) of 16 April 2016 from teleseismic and tsunami data. *Geophysical Research Letters*, *44*, 2211–2219. doi:10.1002/2017GL072545

Hino, R., Inazu, D., Ohta, Y., Ito, Y., Suzuki, S., Iinuma, T., … Kaneda, Y. (2014). Was the 2011 Tohoku-Oki earthquake preceded by aseismic preslip? Examination of seafloor vertical deformation data near the epicenter. *Marine Geophysical Research*, *35*, 181–190. doi:10.1007/s11001-013-9208-2

Iinuma, T., Hino, R., Kido, M., Inazu, D., Osada, Y., Ito, Y., … Miura, S. (2012). Coseismic slip distribution of the 2011 off the Pacific Coast of Tohoku Earthquake (M9.0) refined by means of seafloor geodetic data. *Journal of Geophysical Research*, *117*, B07409. doi:10.1029/2012JB009186

Inazu, D., & Saito, T. (2014). Two subevents across the Japan Trench during the 7 December 2012 off Tohoku earthquake (Mw 7.3) inferred from offshore tsunami records. *Journal of Geophysical Research: Solid Earth*, *119*, 5800–5813. doi:10.1002/2013JB010892

Ito, A., Fujie, G., Miura, S., Kodaira, S., Kaneda, Y., & Hino, R. (2005). Bending of the subducting oceanic plate and its implication for rupture propagation of large interplate earthquakes off Miyagi, Japan, in the Japan Trench subduction zone. *Geophysical Research Letters*, *32*, L05310. doi:10.1029/2004GL022307

Ito, Y., Sekiguchi, S., Okada, T., Honda, R., Obara, K., & Hori, S. (2006). Performance of regional distance centroid moment tensor inversion applied to the 2004 mid-Niigata prefecture earthquake, Japan. *Geophysical Journal International*, *167*(3), 1317–1331. doi:10.1111/j.1365-246X.2006.03109.x

Ito, Y., Tsuji, T., Osada, Y., Kido, M., Inazu, D., Hayashi, Y., Tsushima, H., Hino, R., & Fujimoto, H. (2011). Frontal wedge deformation near the source region of the 2011 Tohoku-Oki earthquake. *Geophysical Research Letters*, *38*(7), L00G05. doi:10.1029/2011GL048355

Ito, Y., Hino, R., Kido, M., Fujimoto, H., Osada, Y., Inazu, D., … Ashi, J. (2013). Episodic slow slip events in the Japan subduction zone before the 2011 Tohoku-Oki earthquake. *Tectonophysics*, *600*, 14–26. doi:10.1016/j.tecto.2012.08.022

Kanazawa, T., & Hasegawa, A. (1997), *Ocean-bottom observatory for earthquakes and tsunami off Sanriku, north-east Japan using submarine cable*. Paper presented at International Workshop on Scientific Use of Submarine Cables, 208–209, Comm. For Sci. Use of Submarine Cables, Okinawa, Japan.

Kikuchi, M., & Kanamori, H. (1991). Inversion of complex body waves—III. *Bulletin of the Seismological Society of America*, *81*(6), 2335–2350.

Kozdon, J. E., & Dunham, E. M. (2014). Constraining shallow slip and tsunami excitation in megathrust ruptures using seismic and ocean acoustic waves recorded on ocean-bottom sensor networks. *Earth and Planetary Science Letters*, *396*, 56–65. doi:10.1016/j.epsl.2014.04.001

Kubo, A., Fukuyama, E., Kawai, H., & Nonomura, K. (2002). NIED seismic moment tensor catalogue for regional earthquakes around Japan: Quality test and application. *Tectonophysics*, *356*, 23–48. doi:10.1016/S0040-1951(02)00375-X

Kubota, T., Hino, R., Inazu, D., Ito, Y., & Iinuma, T. (2015). Complicated rupture process of the Mw 7.0 intraslab strike-slip earthquake in the Tohoku region on 10 July 2011 revealed by near-field pressure records. *Geophysical Research Letters*, *42*, 9733–9739. doi:10.1002/2015GL066101

Kubota, T., Hino, R., Inazu, D., Ito, Y., Iinuma, T., Ohta, Y., … Suzuki, K. (2017). Coseismic slip model of offshore moderate interplate earthquakes on March 9, 2011 in Tohoku using tsunami waveforms. *Earth and Planetary Science Letters*, *458*, 241–251. doi:10.1016/j.epsl.2016.10.047

Maeda, T., Furumura, T., Noguchi, S., Takemura, S., Sakai, S., Shinohara, M., … Lee, S.-J. (2013). Seismic- and Tsunami-wave propagation of the 2011 Off the Pacific Coast of Tohoku earthquake as inferred from the Tsunami-coupled finite-difference simulation. *Bulletin of the Seismological Society of America*, *103*(2B), 1456–1472. doi:10.1785/0120120118

Matsumoto, H., Inoue, S., & Ohmachi, T. (2012). Dynamic Response of Bottom Water Pressure due to the 2011 Tohoku Earthquake. *Journal of Disaster Research*, *7*, 468–475. doi:10.20965/jdr.2012.p0468

National Research Institute for Earth Science and Disaster Resilience (2011a). *F-net Broadband Seismograph Network: Earthquake Mechanism Information*. Retrieved 21

August 2011, from http://www.fnet.bosai.go.jp/event/tdmt.php?_id=20110309024400&LANG=en

National Research Institute for Earth Science and Disaster Resilience (2011b). *F-net Broadband Seismograph Network: Earthquake Mechanism Information*. Retrieved 21 August 2011, from http://www.fnet.bosai.go.jp/event/tdmt.php?_id=20110309212200&LANG=en

Nosov, M. A., & Kolesov, S. V. (2007). Elastic oscillations of water column in the 2003 Tokachi-oki tsunami source: in-situ measurements and 3-D numerical modelling. *Natural Hazards and Earth System Science*, *7*, 243–249. doi:10.5194/nhess-7-243-2007

Ohta, Y., Hino, R., Inazu, D., Ohzono, M., Ito, Y., Mishina, M., … Miura, S. (2012). Geodetic constraints on afterslip characteristics following the March 9, 2011, Sanriku-oki earthquake, Japan. *Geophysical Research Letters*, *39*, L16304. doi:10.1029/2012GL052430

Okada, Y., Kasahara, K., Hori, S., Obara, K., Sekiguchi, S., Fujiwara, H., & Yamamoto, A. (2004). Recent progress of seismic observation networks in Japan - Hi-net, F-net, K-NET and KiK-net. *Earth Planets and Space*, *56*(8), xv–xxviii. doi:10.1186/BF03353076

Saikia, C. K. (1994). Modified frequency-wavenumber algorithm for regional seismograms using Filon's quadrature: modelling of Lg waves in eastern North America. *Geophysical Journal International*, *118*, 142–158. doi:10.1111/j.1365-246X.1994.tb04680.x

Saito, T. (2013). Dynamic Tsunami generation due to sea-bottom deformation: Analytical representation based on linear potential theory. *Earth, Planets and Space*, *65*, 1411–1423. doi:10.5047/eps.2013.07.004

Saito, T. (2017). Tsunami Generation: Validity and limitations of conventional theories. *Geophysical Journal International*, *210*, 1888–1900. doi:10.1093/gji/ggx275

Saito, T., & Tsushima, H. (2016). Synthesizing ocean bottom pressure records including seismic wave and tsunami contributions: Toward realistic tests of monitoring systems.

Journal of Geophysical Research: Solid Earth, *121*, 8175–8195. doi:10.1002/2016JB013195

Saito, T., Satake, K., & Furumura, T. (2010). Tsunami waveform inversion including dispersive waves: The 2004 earthquake off Kii Peninsula, Japan. *Journal of Geophysical Research*, *115*, B06303. doi:10.1029/2009JB006884

Suzuki, K., Hino, R., Ito, Y., Yamamoto, Y., Suzuki, S., Fujimoto, H., … Kaneda, Y. (2012). Seismicity near the hypocenter of the 2011 off the Pacific coast of Tohoku earthquake deduced by using ocean bottom seismographic data. *Earth, Planets and Space*, *64*, 1125–1135. doi:10.5047/eps.2012.04.010

Tsushima, H., Hino, R., Tanioka, Y., Imamura, F., & Fujimoto, H. (2012). Tsunami waveform inversion incorporating permanent seafloor deformation and its application to tsunami forecasting. *Journal of Geophysical Research*, *117*, B03311. doi:10.1029/2011JB008877

Wallace, L. M., Araki, E., Saffer, D., Wang, X., Roesner, A., Kopf, A., … Carr, S. (2016). Near-field observations of an offshore Mw 6.0 earthquake from an integrated seafloor and subseafloor monitoring network at the Nankai Trough, southwest Japan. *Journal of Geophysical Research: Solid Earth*, *121*, 8338–8351. doi:10.1002/2016JB013417

Wessel, P., & Smith, W. H. F. (1998). New, improved version of generic mapping tools released. *Eos, Transactions American Geophysical Union*, *79*(47), 579–579. doi:10.1029/98EO00426

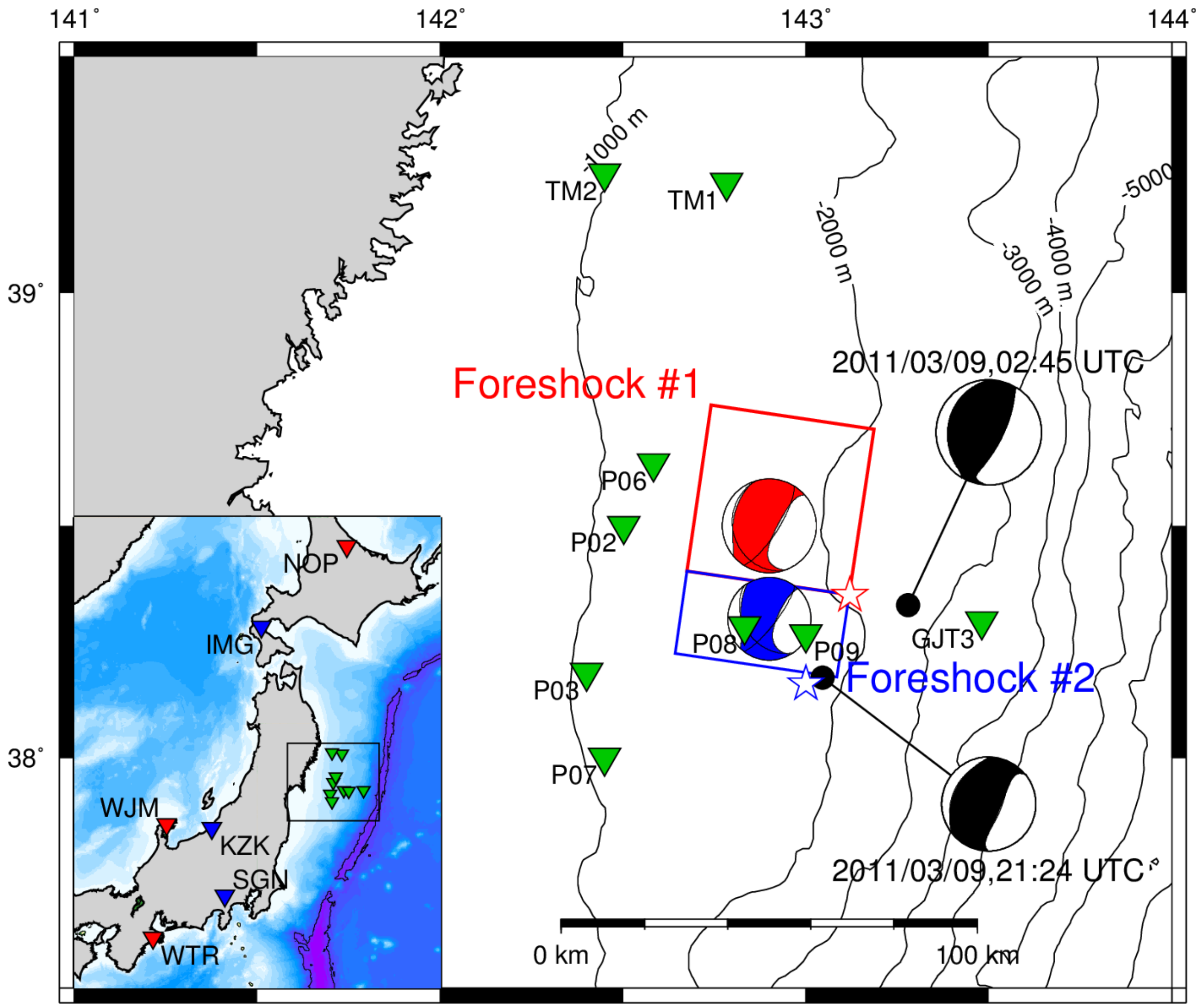

Figure 1. Location map of this study. Stars are the epicenters determined from ocean bottom seismographs (Suzuki et al., 2012), and rectangles are coseismic rupture areas from near-field tsunami analysis (Kubota et al., 2017) (red: foreshock #1, blue: #2). Inverted triangles denote station locations (green: OBPGs, red and blue: F-net broadband seismometers). F-net routine MT solutions (NIED, 2011a; 2011b) are shown in black, and colored CMT solutions are those obtained jointly using onshore and offshore datasets (also shown in Figures 4b and 5b).

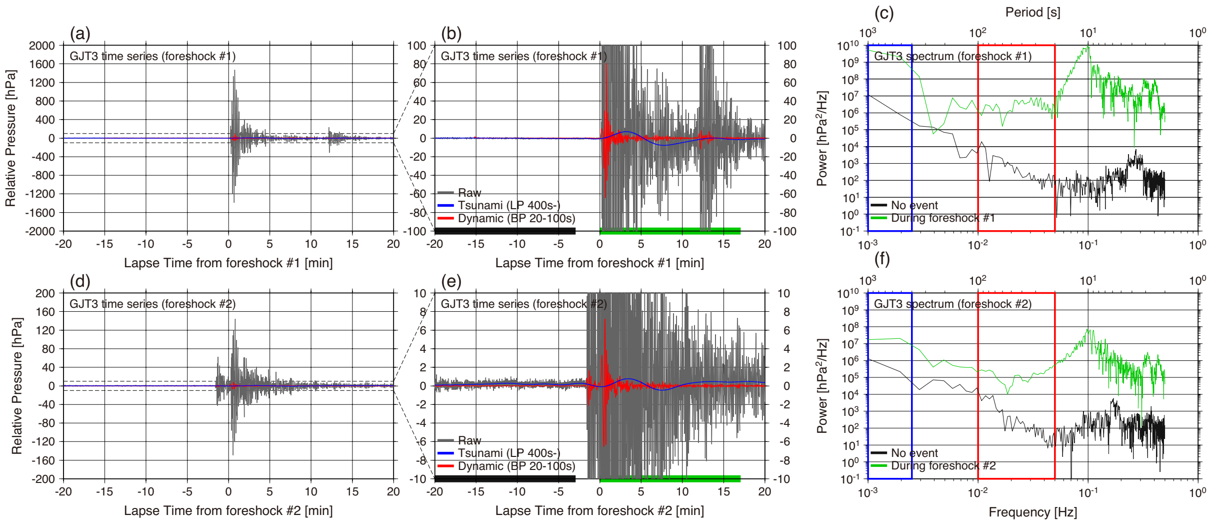

Figure 2. OBPG records of local earthquakes on 9 March 2011 observed at station GJT3 (shown in Figure 1). (a–b) Time series associated with the Mw 7.2 earthquake. Gray, blue, and red lines are the original, low-pass (>400 s), and bandpass filtered (0.01–0.05 Hz) records, respectively. (c) Power spectra during the Mw 7.2 earthquake (green) and calm period (black), calculated from 1024 s time windows marked by colored bars in Figure 2b. Passbands of the filter in Figure 2b are marked by colored rectangles. (d–f) Time series and power spectra of the Mw 6.5 earthquake.

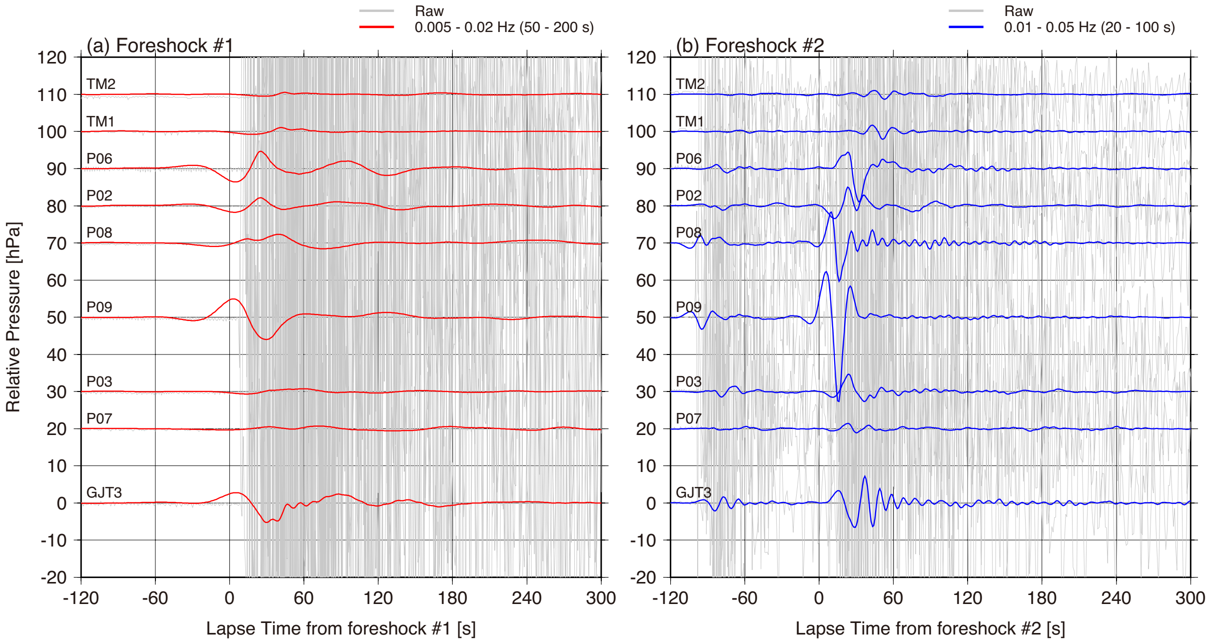

Figure 3. Comparison of raw pressure waveforms (gray) and bandpass filtered waveforms for (a) foreshocks #1 and (b) #2.

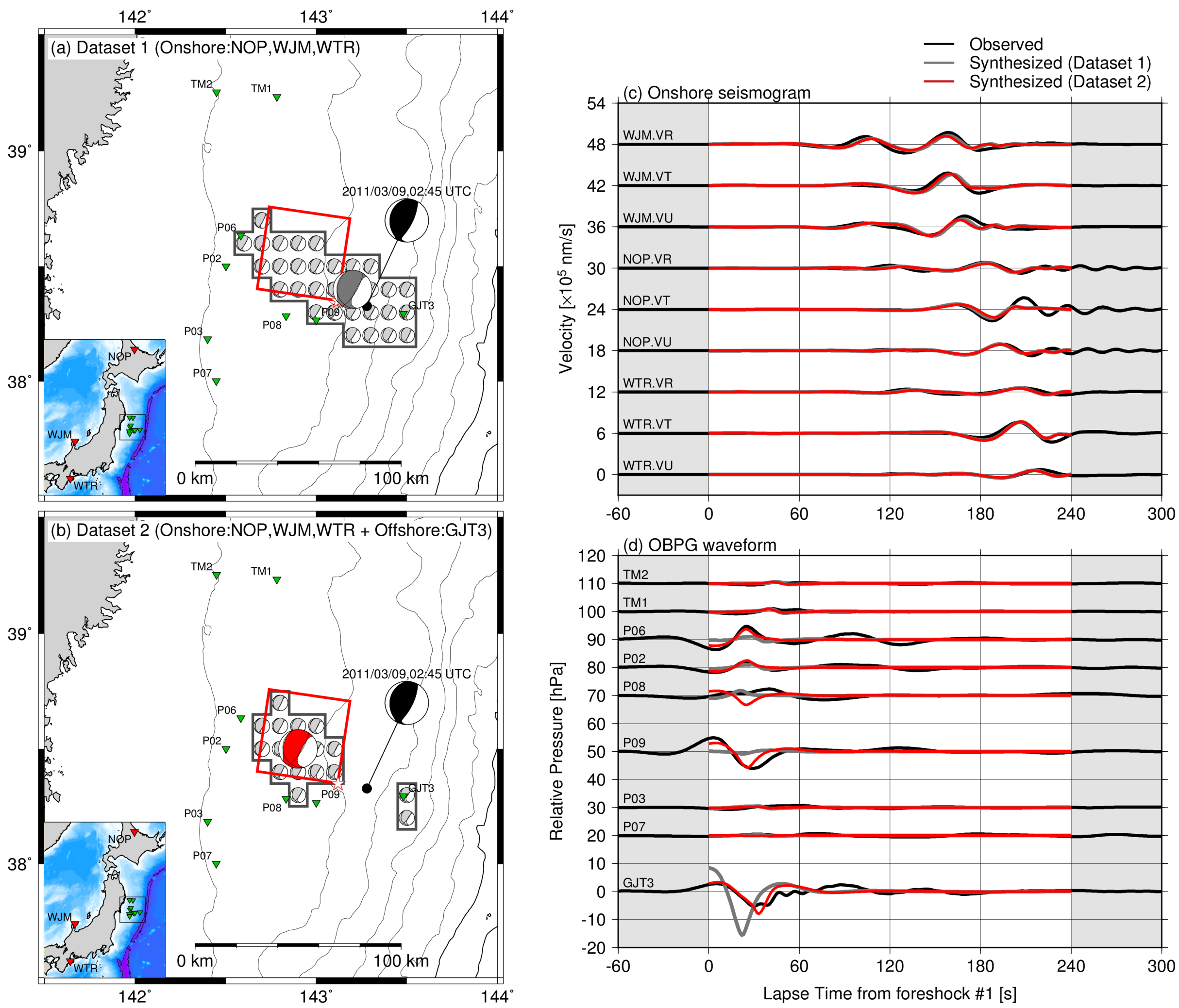

Figure 4. CMT inversion of foreshock #1. (a) Result obtained from dataset 1, only onshore seismometers (NOP, WJM, and WTR). The best-fit solution is in gray. (b) Result obtained from dataset 2, jointly using onshore seismometers and OBPGs (NOP, WJM, WTR, and GJT3). The best-fit solution is in red. Thick gray lines and small CMTs denote area where the calculated VR exceeds 90% of the best-fit VR. (c) Comparison of onshore seismograms. (d) Comparison of OBPG waveforms, between observed waveforms (black), and synthesized waveforms calculated from the best-fit solution obtained from datasets 1 (gray) and 2 (red), respectively. A time window of 0–240 s (white background area) was used for inversion.

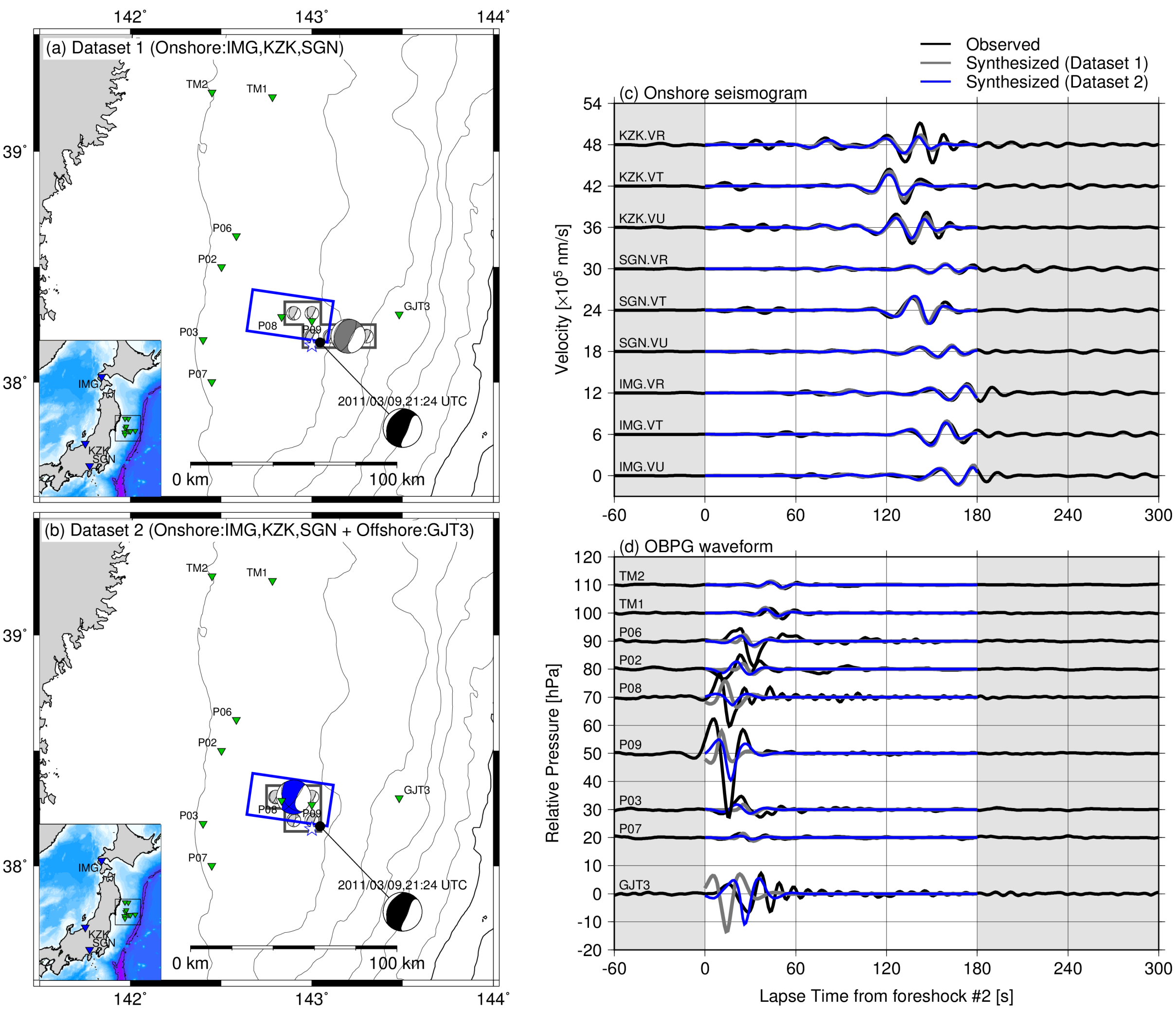

Figure 5. CMT inversion of foreshock #2. Symbols and colors are the same as in Figure 4.

Geophysical Research Letters

Supporting Information for

Estimation of seismic centroid moment tensor using ocean bottom pressure gauges as seismometers

Tatsuya Kubota[1], Tatsuhiko Saito[1], Wataru Suzuki[1], and Ryota Hino[2]

[1]National Research Institute for Earth Science and Disaster Resilience, Tsukuba, Japan.

[2]Graduate School of Science, Tohoku University, Sendai, Japan.

Contents of this file

Introduction

Text S1 describes the method to estimate the centroid moment tensor by waveform inversion. The description for the supplementary datasets (Datasets S1, S2, and S3) is in Text S2. Figure S1 is the vertical distribution of moment tensor solutions to evaluate the resolution of the centroid depth. Table S1 gives the locations of the OBPG stations. The seismic structure used for calculation of the dynamic pressure is shown in Table S2.

Text S1.

In this study, the centroid moment tensors, centroid times, and centroid locations were estimated using the grid-search approach of Ito et al. (2006), under the assumption that the source can be represented by a point source. Here, the detail of the procedure is described.

By assuming the target events is represented by a pure deviatoric moment tensor (MT) without an isotropic component, the observation equation is expressed as:

$$\mathbf{w}^{\mathrm{T}}\mathbf{d} = \mathbf{w}^{\mathrm{T}}\mathbf{G}\mathbf{m}, \tag{S1}$$

where **w** is the vector representing the weight of the data, **d** is the data vector, **G** is the matrix composed of the Green's function, and **m** is the model parameter vector consisting of five independent basis MT components (e.g., Kikuchi & Kanamori, 1991). Note that the onshore seismometers and offshore OBPGs have different dimensions. To reduce the bias caused by the difference in the inversion analysis, we introduced the weight value w_k (k-th datum of the weight vector **w**):

$$w_k = \frac{1}{\max(d_i(t))}, \tag{S2}$$

where $d_i(t)$ is the time series of the i-th station including the k-th datum. From equation (S1), we obtain the model parameter vector as:

$$\mathbf{m} = [\mathbf{G}^{\mathrm{T}}\mathbf{w}\mathbf{w}^{\mathrm{T}}\mathbf{G}]^{-1}\mathbf{G}^{\mathrm{T}}\mathbf{w}\mathbf{w}^{\mathrm{T}}\mathbf{d}. \tag{S3}$$

We used a time window of 0–240 s from the focal time determined from the ocean bottom seismometers (Suzuki et al., 2012) for foreshock #1, and 0–180 s for foreshock #2, taking their magnitudes and the time windows used in the F-net MT analysis into account.

In the analysis, we calculated the Green's function using the discrete wavenumber frequency method with a 1-D subsurface structure (e.g., Saikia, 1994). Table S2 gives the seismic velocity, attenuation, and density structure used for the calculation, which are the same as those used in the F-net moment tensor calculation, and considered suitable for the 1-D structure of inland Japan (Kubo et al., 2002). Note that we did not assume the effect of the sedimentary layer and the topography for simplicity (i.e., OBPGs are assumed to be located on hard rock on the sea surface). We assumed an impulsive source time function, and the bandpass filter is applied as that used for the observation. Finally, the calculated seafloor vertical acceleration is converted to the dynamic pressure change using the pressure–acceleration relationship $p = \rho_0 h_0 a_z$ (equation (1)), assuming the water density ρ_0 is 1.03 g/cm^3, where a_z is the vertical acceleration. The water depth (h_0) of the OBPGs are summarized in Table S1. The same bandpass filters used in the dynamic pressure records are also applied to the Green's function. After we obtained the best fit CMT solution, we forwardly calculated the waveforms which are not used for the inversion analysis to compare with the observation, using the superposition of the Green's functions calculated from five independent basis MT components.

Text S2.

The 1-s sampled raw pressure data used in this study are available in supplementary datasets S1, S2, and S3. This text describes the contents of the datasets.

Dataset S1 is the raw pressure time series for both foreshocks at GJT3, with the time window of -20 min to 20 min from the focal time. This dataset was used to prepare Figure 2. Note that both datasets contain the ocean tide components, although tides were removed in the time series shown in Figure 2 (detail of the tide removal procedure is in Kubota et al. (2017)). The first column denotes the lapse time from the focal time (02:45:16 UTC on 9 March 2011 for foreshock #1 and 21:24:01 UTC for foreshock #2), determined by Suzuki et al. (2012). Times of day (hour, minute, and second in UTC) for both events are also shown.

Datasets S2 and S3 are the raw pressure data for foreshocks #1 and #2, respectively. These datasets were used to prepare Figures 3, 4, and 5. The formats of the time stamps are the same as Dataset S1. The names of the OBPG stations are shown in the first row.

We note that the deployment and retrieval of the OBPGs at GJT3, P02, P03, P06, P07, P08, and P09 were conducted by Tohoku University (Hino et al., 2014; Kubota et al., 2017), and the real-time cabled OBPGs at TM1 and TM2 were operated by Earthquake Research Institute (ERI) of the University of Tokyo (Kanazawa & Hasegawa, 1998). The TM1/TM2 data were resampled to 1 s, although the sampling rate of the original ones was 10 Hz.

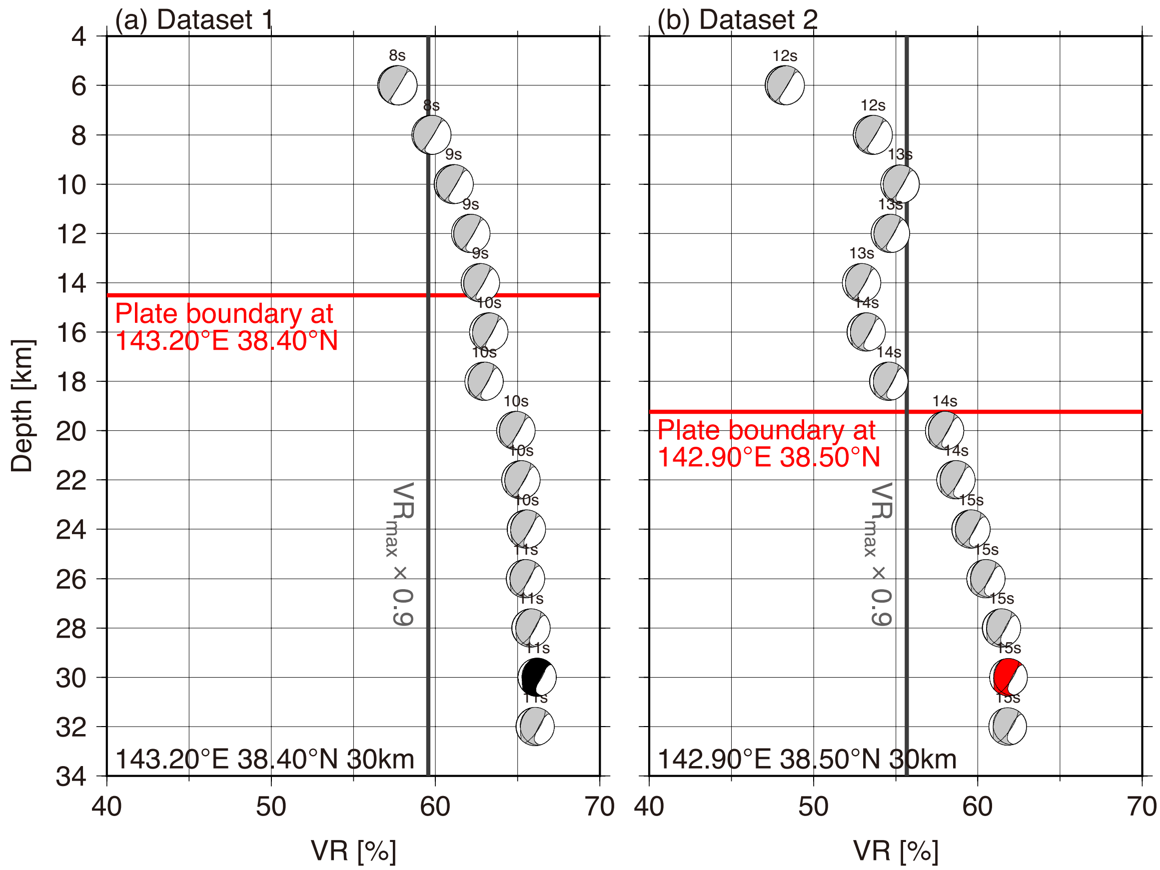

Figure S1. Vertical distribution of VRs and moment tensors at the horizontal location of the best-fit CMT solution for foreshock #1 (Figure 4). (a) Result from dataset consisting of only the onshore seismograms (Figure 4a). (b) Result from dataset consisting of onshore seismograms and offshore pressure data (Figures 4b). The location of the best-fit centroid is shown in the bottom left in each figure. Horizontal and vertical axes denote VR and centroid depth, respectively. Small numbers above each solution are the centroid time delay from the focal time. Red lines denote plate boundary depths obtained from seismic surveys by Ito et al. (2005).

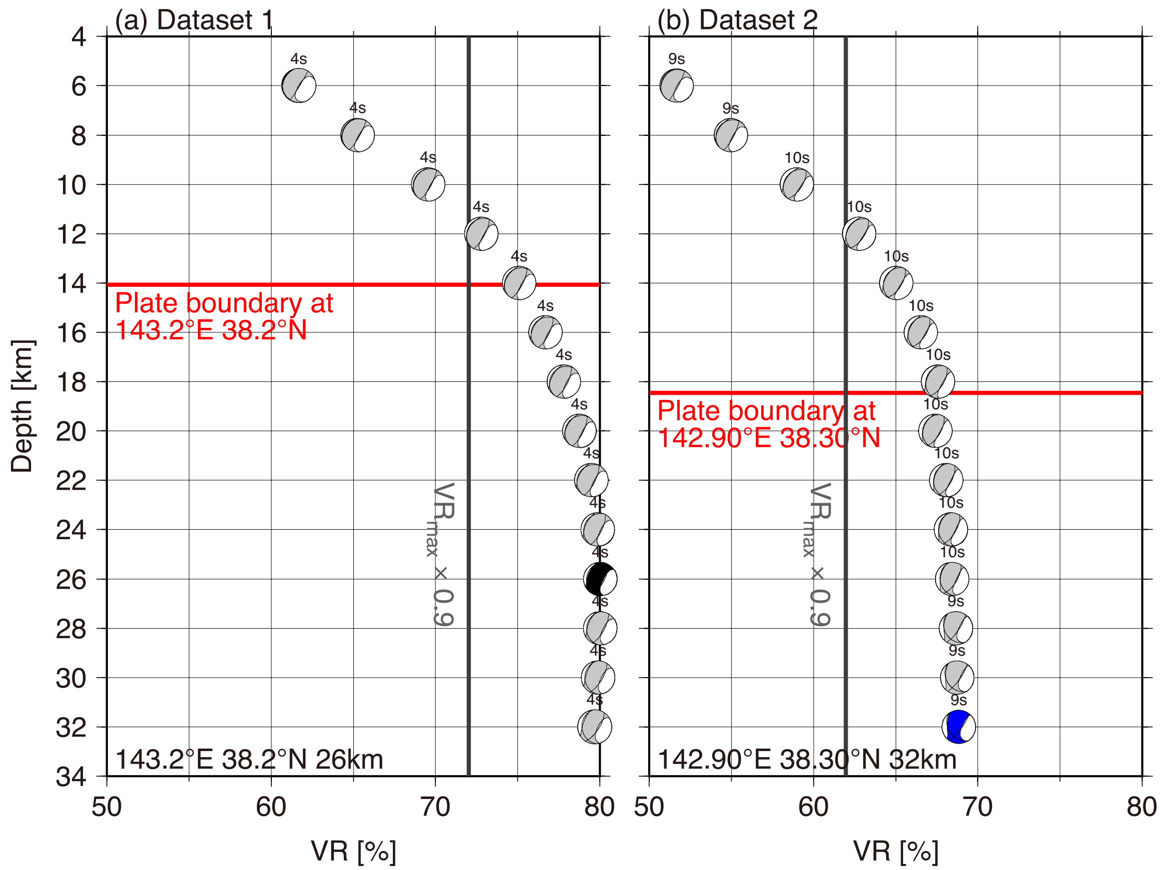

Figure S2. Vertical distribution of VR and moment tensors at the horizontal location of the best-fit CMT solution for foreshock #2 (Figure 5). (a) Result from dataset consisting of only onshore seismograms (Figure 5a). (b) Result from dataset consisting of onshore seismograms and offshore pressure data (Figures 5b). The location of the best-fit centroid is shown in the bottom left in each figure. Horizontal and vertical axes denote VR and centroid depth, respectively. Small numbers above each solution are the centroid time delay from the focal time. Red lines denote plate boundary depths obtained from seismic surveys by Ito et al. (2005).

Table S1. Locations of OBPGs

Station	Latitude [°N]	Longitude [°E]	Depth [m]
GJT3[a]	38.2945	143.4814	3,293
P02[a]	38.5002	142.5016	1,104
P03[a]	38.1834	142.3998	1,052
P06[a]	38.6340	142.5838	1,254
P07[a]	38.0003	142.4488	1,059
P08[a]	38.2855	142.8330	1,418
P09[a]	38.2659	143.0006	1,556
TM1[b]	39.2330	142.7830	1,564
TM2[b]	39.2528	142.4500	954

[a]Pop-up recovery OBPG identical to those used in Hino et al. (2014) and Kubota et al. (2017)
[b]Real-time cabled observation systems operated by the Earthquake Research Institute (ERI) of the University of Tokyo (Kanazawa & Hasegawa, 1997)

Table S2. Structure model used in this study[a]

Depth [km]	Thickness [km]	P-wave velocity [km/s]	S-wave velocity [km/s]	Density [kg/m^3]	Qp	Qs
0	3	5.50	3.14	2300	600	300
3	15	6.00	3.55	2400	600	300
8	15	6.70	3.83	2800	600	300
18	67	7.80	4.46	3200	600	300
33	125	8.00	4.57	3300	600	300
100	100	8.40	4.80	3400	600	300
225	100	8.60	4.91	3500	600	300
425	—	9.30	5.31	3700	600	300

[a]This structure is same as that used in the F-net MT calculation and considered to be suitable for the one-dimensional structure of inland Japan (Kubo et al., 2002).